



Highly crystalline carbon nitrogen polymer with a strong built-in electric fields for ultra-high photocatalytic H₂O₂ production

Liang Jian ^a, Yuming Dong ^{a,*}, Hui Zhao ^a, Chengsi Pan ^a, Guangli Wang ^a, Yongfa Zhu ^{a,b,**}

^a International Joint Research Center for Photo-responsive Molecules and Materials, School of Chemical and Material Engineering, Jiangnan University, Wuxi 214122, China

^b Department of Chemistry, Tsinghua University, Beijing 100084, China



ARTICLE INFO

Keywords:

Photocatalysis
Hydrogen peroxide (H₂O₂)
Highly crystalline
Carbon nitride polymer
Built-in electric field

ABSTRACT

Efficient photogenerated charge separation and rapid migration provide more charges for surface redox reactions. Herein, the carbon nitride polymer with highly crystalline is prepared for efficient photocatalytic H₂O₂ generation. The strong built-in electric field induced by its high crystallinity is beneficial for promoting exciton dissociation, resulting in a surface photovoltage of 19.24 mV. Meanwhile, the formed nanocrystals shorten the charge migration distance to facilitate photogenerated charge rapid migration. The abundant surface –C≡N/–OH groups provide more active sites for the adsorption of O₂. As a result, the photocatalytic H₂O₂ production rate (16.01 mmol•L⁻¹•h⁻¹•g⁻¹) under visible light ($\lambda > 400$ nm) was increased 77-fold relative to pristine graphitic carbon nitride, with a quantum efficiency of 25.1% at 405 nm. The photocatalytic H₂O₂ production reached 80.36 mM after 8 h. The highly crystalline carbon nitride polymer throws prospect on photocatalytic H₂O₂ production, showing a new perspective for the design of photocatalysts.

1. Introduction

Hydrogen peroxide (H₂O₂) has attracted significant attention as an efficient and environmentally-friendly oxidant and sustainable energy carrier with the highest reactive oxygen content (47.1 wt%), which is applied in organic synthesis, wastewater treatment, medical disinfection, fuel cell, and paper industries, among others [1,2]. The traditional anthraquinone method for producing H₂O₂ requires large amounts of energy and resources, and produces a large amount of toxic waste liquid that is harmful to the ecological environment [3]. Compared with the anthraquinone method, the photocatalytic two-electron (2e⁻) oxygen reduction reaction (ORR) to generate hydrogen peroxide (H₂O₂) is a mild, sustainable, energy-saving, safe and green synthesis method [4–11]. However, due to the low conversion efficiency of the photocatalytic reduction of two-electron (2e⁻) O₂ to H₂O₂, the rapid generation of H₂O₂ still faces a great challenge. Effective exciton dissociation generates electrons and holes. Meanwhile, the effective separation and rapid transfer of the generated electrons to the catalytic surface sites is a key factor to enhance the rapid conversion of O₂ to H₂O₂. Therefore, it is highly desirable to construct semiconductor materials with high surface charge density for the rapid conversion of photocatalytic reduction of O₂

to H₂O₂.

Up to now, carbon nitride polymer (PCN) has been extensively studied for its potential in photocatalytic H₂O₂ production due to its high stability, suitable energy band structure and electronic structure [12,13]. However, the Frenkel excitons of PCN exhibit strong intrinsic Coulomb interactions and large exciton binding energies (0.1–1.0 eV), which make it difficult for the exciton to dissociate, resulting in poor photogenerated charge separation efficiency [14–18]. In addition, incomplete polymerization of PCN produces a large number of structural defects that severely inhibit in-plane charge transfer efficiency [19,20]. Meanwhile, the weak van der Waals forces between the two-dimensional PCN layers severely inhibit the interlayer charge transport efficiency [21]. As a result, PCN exhibits poor exciton dissociation efficiency and photogenerated charge separation efficiency, leading to low surface charge density and photocatalytic performance. To promote the exciton dissociation and photogenerated carrier separation, the construction of the built-in electric field is a useful solution [22–29]. The strong built-in electric field caused by the high crystallinity of the catalyst itself helps to accelerate the exciton dissociation and facilitate the charge separation and transfer from the bulk phase to the surface. Meanwhile, the strategy of surface engineering on catalyst could provide more surface active

* Corresponding author.

** Corresponding author at: Department of Chemistry, Tsinghua University, Beijing 100084, China.

E-mail addresses: dongym@jiangnan.edu.cn (Y. Dong), zhuyf@tsinghua.edu.cn (Y. Zhu).

sites for photocatalytic O_2 reduction to H_2O_2 . Therefore, the construction of carbon nitrogen polymer with in-plane highly crystalline and abundant superficial active sites is expected to achieve a breakthrough in the rapid conversion of photocatalytic reduction O_2 to H_2O_2 .

Based on the above considerations, carbon nitride polymer photocatalysts with high crystallinity were prepared in this work by sodium chloride-assisted calcination on triamino-s-heptazine (Melem) (**Scheme 1**). It is noteworthy that the surface $-C\equiv N/-OH$ groups were successfully introduced into carbon nitride polymer. In addition, the robust built-in electric field induced by its high crystallinity is beneficial for promoting exciton dissociation, accelerating photogenerated carrier separation and transfer from the bulk phase to the surface, resulting in a surface photovoltage of up to 19.24 mV. Meanwhile, the abundant surface $-C\equiv N/-OH$ groups provide more active sites for the adsorption reduction of O_2 . The results show that the photocatalytic H_2O_2 production rate reached $16.01 \text{ mmol} \cdot L^{-1} \cdot h^{-1} \cdot g^{-1}$ under visible light, with a quantum efficiency of 25.1% at 405 nm. The H_2O_2 concentration reached 80.36 mM after 8 h of photocatalytic reaction under simulated sunlight. This study provides a new insight into the design of photocatalytic systems with high crystallinity and the mechanism of photocatalytic $2e^-$ ORR reaction for H_2O_2 production.

2. Materials and methods

2.1. Chemicals and reagents

Melamine ($C_3H_6N_6$, 99.0%, Sinopharm), Sodium chloride (NaCl, 99.5%, Sinopharm), Methanol (CH_3OH , 99.5%, Sinopharm), Ethanol (C_2H_5OH , 95.0%, Sinopharm), Ethylene glycol ($C_2H_6O_2$, 99%, Sinopharm), Isopropyl alcohol (C_3H_8O , 99.7%, Sinopharm), Glycerol ($C_3H_8O_3$, 99.7%, Sinopharm), 4-Chlorophenol (C_6H_5OCl , 99.0%, Sinopharm), Formic acid ($HCOOH$, 85.0%, Sinopharm), 5-hydroxymethylfurfural ($C_6H_6O_3$, AR, Sinopharm), Potassium iodide (KI, 99.0%, Sinopharm), Potassium hydrogen phthalate ($C_8H_5O_4K$, 99.8%, Sinopharm), P-benzoquinone ($C_6H_4O_2$, 98.0%, Sinopharm), Silver nitrate ($AgNO_3$, AR, Sinopharm), Hydrochloric acid (HCl, AR, Sinopharm), Sodium hydroxide (NaOH, AR, Sinopharm). The above reagents can be used directly without further purification.

2.2. Synthesis of photocatalysts

Melem was obtained according to the previously reported preparation method.^[31] Briefly, 6 g of melamine was placed in a porcelain boat with a lid. Then it was heated up to 425 °C under N_2 atmosphere at a heating rate of 2 °C/min and kept for 4 h to obtain Melem. 2 g of Melem and a certain amount of NaCl (5 g, 10 g and 15 g) were placed into a

ball-milled zirconium jar and ball-milled for 30 min to obtain a solid mixture. The mixture was placed in a porcelain boat with a lid, under N_2 atmosphere, and heated to 570 °C at a heating rate of 2 °C/min and held for 4 h to obtain a yellow solid. Then the yellow solid was dispersed into deionized water and washed ultrasonically several times, and finally filtered to obtain carbon nitride polymer (Na-PCN-570 °C) yellow powder. According to calculations, the yield of the material is approximately 72%. The above steps were repeated to prepare Na-PCN-X at different temperatures by adjusting the retention temperature to 500 °C, 520 °C, 540 °C, 550 °C, 570 °C and 600 °C (X stands for temperature). Preparation of pristine carbon nitride (PCN): 2 g of Melem was put into a porcelain boat with a lid, under N_2 atmosphere, and heated to 550 °C and kept for 4 h with a heating rate of 2 °C/min to obtain a light-yellow solid.

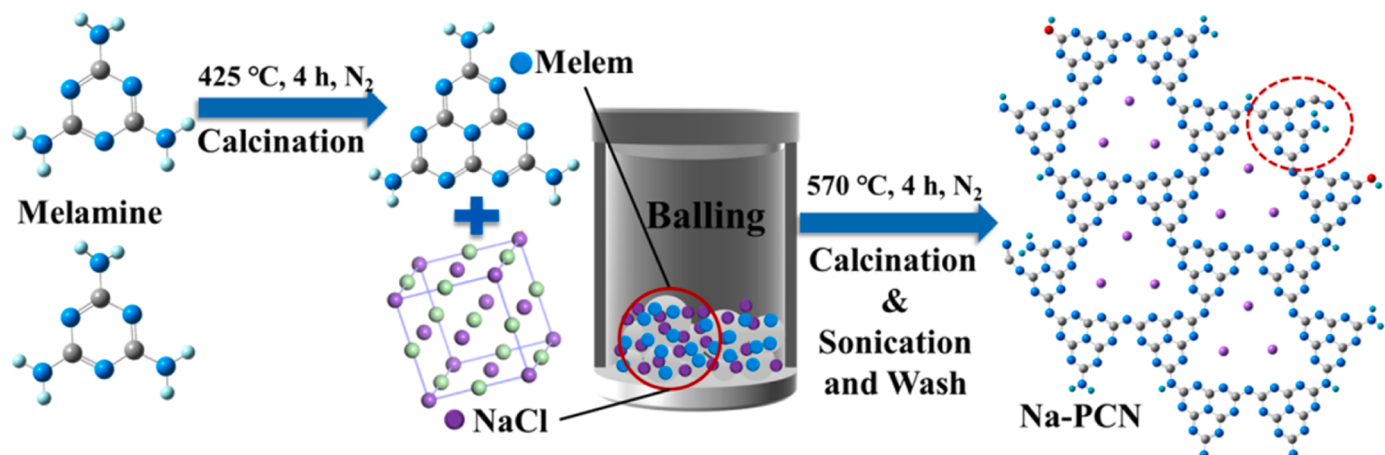
2.3. Photocatalytic reduction of O_2 to H_2O_2

The prepared material of 50 mg was ultrasonically dispersed in a 50 mL aqueous solution of 10% ethanol and stirred in the dark for 30 min with a certain flow of oxygen to reach the O_2 adsorption-desorption equilibrium. Then, the reactor temperature was maintained at 25 °C by a condensing unit, and photocatalytic H_2O_2 production experiments were performed under a 300 W xenon lamp (equipped with a $\lambda > 400$ nm filter as the lamp source). During the reaction, 3 mL of suspension was collected every 15 min and the photocatalyst material was removed using a 0.22 μ L (13 mm) nylon pinhead filter. The H_2O_2 concentration was measured by the iodination method. Repeating the above process, we performed photocatalytic H_2O_2 production experiments under the absence of a sacrificial agent. In addition, the photocatalytic H_2O_2 production activity under different sacrificial agents (methanol, isopropanol, ethylene glycol and glycerol), in different pH environments and in aqueous formic acid solutions was also investigated. Free radical scavenger quenching experiment is achieved by adding different free radical scavengers in the photocatalytic H_2O_2 production process, including p-benzoquinone (PBQ) for $\cdot O_2^-$, N_2 for O_2 and $AgNO_3$ for e^- .

3. Results and discussion

3.1. Structural characterization of highly crystalline carbon nitride polymer

Highly crystalline carbon nitride polymer (denoted as Na-PCN) was prepared by polymerization of Melem on the surface of NaCl crystals at high temperature (**Scheme 1**). The structure of Melem was confirmed by FT-IR and XRD spectra (Fig. S1). NaCl crystals with relatively high



Scheme 1. The synthesis schematic diagram of Na-PCN.

surface energy help to reduce the kinetic potential barrier for Melem condensation reactions on their surface [19]. At the same time, the unique interaction between NaCl crystals and Melem leads to strong interfacial confinement, which promotes the directed assembly of two-dimensional nanosheets on the crystal plane. In addition, Na^+ is doped into the carbon nitride polymer matrix to provide a stable structural base site for Na-PCN [30,31]. Thus, after removal of NaCl crystals by aqueous washing, Na-PCN with high crystalline structure can be obtained, especially with in-plane long-range ordering between heptazine units.

The XRD spectrum of Na-PCN (Fig. 1a) shows distinct diffraction peaks at 14.4° , 22.0° , 26.7° , 28.9° , 30.1° and 36.6° , respectively corresponding to the (110), (210), (002), (220), (310) and (320) lattice planes of the carbon nitride polymer structure, respectively, indicating its high crystallinity. The crystallinity of Na-PCN was influenced by the calcination temperature as evidenced by the XRD pattern (Fig. S2b). In particular, compared to PCN (Fig. S2a), Na-PCN has a stronger diffraction peak at 8.3° , which is attributed to the in-plane long-range ordered (100) lattice plane between the heptazine units. Moreover, Na-PCN presents a broader and weaker (002) diffraction peak at 26.7° , which

is caused by the stacking reflection of interlayer toward a reduced dimensional structure and alkali metal Na^+ doping, indicating that thin nanosheets can be formed by the on-surface polymerization method [19]. The (002) lattice plane of PCN (Fig. S4) and the lattice stripes of Na-PCN can be observed by HR-TEM (Fig. 1d-e and S3). The lattice stripes with an average d -spacing of 1.02 nm are attributed to the (100) lattice plane of Na-PCN. The (110), (100), (002) lattice planes and the perfect hexagonal distribution of Na-PCN observed by the FFT patterns. In addition, the SAED plot corresponding to Fig. 1b shows the crystallographic characteristics of Na-PCN (Fig. 1c). Meanwhile, the intensity distribution of SAED is consistent with the XRD data, indicating the strong texture of the crystal and the general arrangement of the a-b plane perpendicular to the electron beam direction as well as the highly ordered and crystalline structure of Na-PCN [32–35]. The HR-TEM and XRD data show that the ideal Na-PCN structure crystallizes in the P31m (157) space group in a triangular cell symmetry model, forming a poly-(heptazine imide) structure similar to the "graphite" two-dimensional framework (Fig. 1f), and is consistent with the hexagonal arrangement of the triangular holes and the two-dimensional network topology [36]. The uniform distribution of C, N, O, and Na was observed by elemental

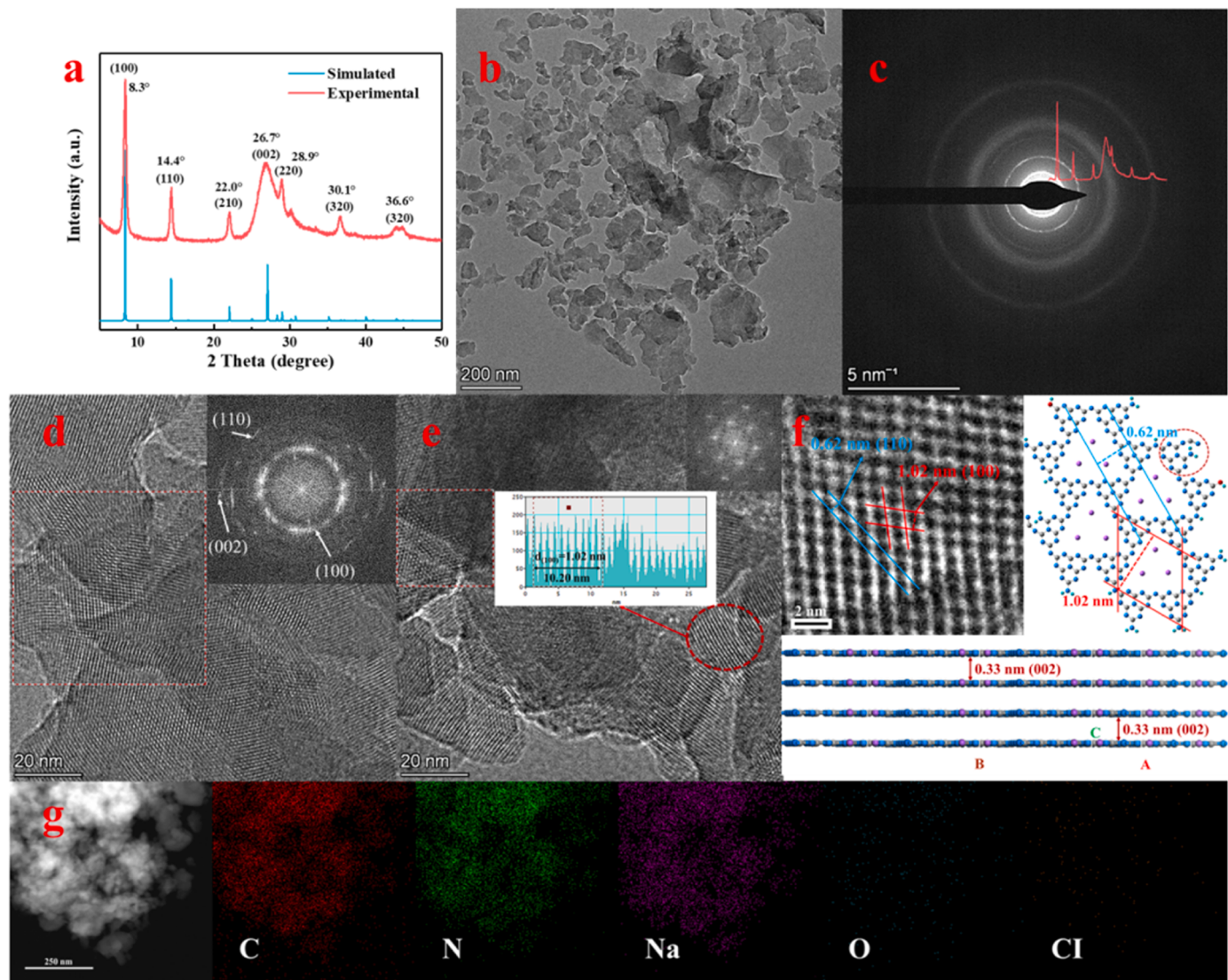


Fig. 1. (a) X-ray diffraction spectra (XRD) of Na-PCN; (b) and (c) Transmission electron micrographs (TEM) of Na-PCN and selected area electron diffraction (SAED); (d) and (e) High resolution TEM (HR-TEM) of Na-PCN (insets show the fast Fourier transform (FFT) patterns and lattice stripe distributions); (f) HR-TEM of Na-PCN, and in-plane and laminar structures based on the theoretical triangular cell model described by XRD, HR-TEM and FFT patterns; (g) Elemental mapping of Na-PCN with C (red), N (green), Na (purple), O (blue), and Cl (yellow).

mapping. Meanwhile, negligible distribution of Cl elements is detected (Fig. 1g and Table S1). Thus, Na-PCN with high crystalline structure can be obtained, especially with in-plane long-range ordering between heptazine units, which facilitates the construction of a strong built-in electric field. Besides, the prepared Na-PCN were observed by TEM to exhibit a small and thin nanosheet distribution or stacked morphology (Figs. S3 and 1b). Furthermore, it was further demonstrated by AFM (Fig. S5-S6) that Na-PCN has a thin nanosheet structure compared to PCN and an average nanosheet thickness of about 1 nm. Therefore, Na-PCN exhibited a larger specific surface area (Fig. S7), which facilitated the exposure of surface-active sites. In addition, Na-PCN has high dispersion and hydrophilicity in water confirmed by contact angle and free deposition experiments (Fig. S8), which is beneficial for the adsorption of dissolved oxygen and protons to promote H₂O₂ production.

The fundamental structural changes of the carbon nitride polymer were investigated by FT-IR and Raman spectroscopy in comparison with PCN (Fig. 2a-b and S9). It is noteworthy that the contraction vibration peak at $\sim 2178\text{ cm}^{-1}$ is attributed to the cyano ($-\text{C}\equiv\text{N}$), which originates from the protonation of terminal C-NH₂ groups. The FT-IR peaks at about 3419 and 1108 cm^{-1} are assigned to $-\text{OH}$ and C-O stretching vibrations. The vibrational peaks at 990 and 1141 cm^{-1} originate from the symmetric and asymmetric vibrations of the N-C₂ bond of the NaN-C₂ group [37,38]. The Raman spectra of PCN (Fig. 2b) show peaks at about 473 cm^{-1} , 707 cm^{-1} and 978 cm^{-1} corresponding to the in-plane torsional vibration peak, out-of-plane deformation vibration and respiration modes of the heterocyclic ring of heptazine, respectively. The peaks located at about 1232 cm^{-1} and 1560 cm^{-1} correspond to the =C(sp²) bending vibration and the N-C-N symmetric stretching vibration, respectively [39,40]. The Raman spectra of Na-PCN show peaks at about 731 cm^{-1} , 1235 cm^{-1} and 1530 cm^{-1} attributed to the out-of-plane deformation vibration of the heptazine heterocycle, the =C(sp²) bending vibration and the symmetric stretching vibration of N-C-N, respectively. The peaks located at 990 cm^{-1}

and 1160 cm^{-1} may be attributed to the symmetric and asymmetric vibrations of the N-C₂ bond of the NaN-C₂ group. The peaks located at 1107 and 2190 cm^{-1} correspond to the stretching vibrations of C-O and $-\text{C}\equiv\text{N}$, respectively [41,42].

The structure of Na-PCN was further verified by the ¹³C solid-state NMR. Two strong peaks located at 164.6 and 156.7 ppm are observed in the ¹³C spectra of PCN and Na-PCN (Fig. 2c), corresponding to the chemical shifts of C₂N-NH_x (C1) and C₃N (C2) in the heptazine unit, respectively. However, three new resonance peaks in Na-PCN appear at ≈ 116.7 ppm at the C4 site (C≡N), ≈ 171.1 ppm at the C3 site (C-OH) and ≈ 179.8 ppm at the C5 site (C atom adjacent to C≡N) [38]. The basic structure and chemical composition of Na-PCN were further revealed by the XPS analysis (Fig. S10). In particular, the high-resolution C 1 s XPS spectrum shows (Fig. 2e) two new characteristic peaks at 286.3 eV and 287.4 eV attributed to $-\text{C}\equiv\text{N}$ and C-O, respectively, compared to PCN. In the high-resolution N 1 s XPS spectrum (Fig. 2f), the reduced binding energy and peak intensity at 400.1 eV (N-C₃) and the increased peak intensity at 400.9 eV (C-NH_x) of Na-PCN relative to PCN are evidence for the successful introduction of $-\text{C}\equiv\text{N}$ and the C-N-C linkage between the heptazine rings. Furthermore, when compared to PCN, the binding energy of N-C≡N in the C1s XPS spectrum of Na-PCN is shifted towards higher binding energy, while the binding energy of all peaks in the N1s XPS spectrum is shifted towards lower binding energy, indicating the formation of a higher electron density at the nitrogen atoms. This shift could be due to the increased electron delocalization in the Na-PCN basic structure with enhanced structural condensation and the perturbed charge distribution on the basic structure by the introduction of Na [19]. The high-resolution O 1 s XPS spectra (Fig. S11) further confirmed the successful introduction of $-\text{OH}$. Furthermore, the two characteristic peaks of Na at 1071.3 and 496.4 eV correspond to the Na 1 s (Fig. S10a) and Na LK1 oscillations, respectively, indicating that Na⁺ coordinates to N located in the intervals of the heptazine unit [19]. The above results indicate the successful introduction of the surface $-\text{C}\equiv\text{N}/-\text{OH}$ groups and the basic

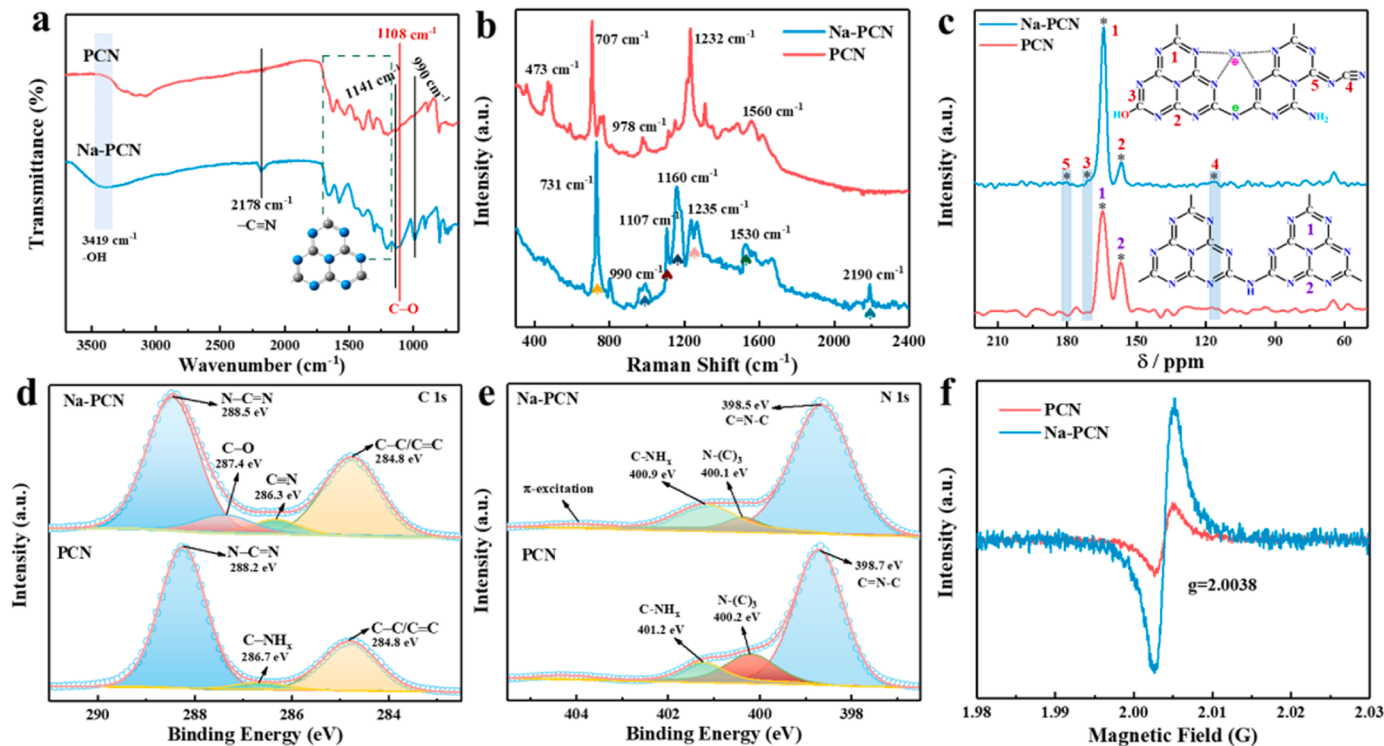


Fig. 2. (a) Fourier transform infrared (FT-IR) spectra of PCN and Na-PCN; (b) Raman spectra of PCN and Na-PCN, respectively, excited at 1064 nm with Nd:YAG excitation source; (c) The ¹³C solid-state nuclear magnetic resonance spectra (NMR) of PCN and Na-PCN; (d) and (e) High-resolution C 1 s and N 1 s XPS of PCN and Na-PCN; (f) Electron paramagnetic resonance (EPR) spectra of PCN and Na-PCN.

framework structure changes of carbon nitride polymer. The EPR spectra (Fig. 2g) of the PCN and Na-PCN show a single Lorentz line and have the same g value ($g = 2.0038$), which is attributed to the unpaired electrons generated by the sp^2 - carbon atom in the π -conjugated aromatic ring. Due to the strong electron-absorbing property of the $-\text{C}\equiv\text{N}$ group leading to the delocalization and concentration of lone pairs of electrons in the π -conjugated heterocycle [43], Na-PCN shows a stronger EPR signal peak. This facilitates the production of photogenerated active radical species, thus enhancing the photocatalytic activity. The highly

crystalline Na-PCN with strong built-in electric field, high hydrophilicity, favorable electronic structure and abundant surface-active sites is highly advantageous for efficient photocatalytic H_2O_2 generation.

3.2. Highly efficient photocatalytic H_2O_2 generation

The highly crystalline Na-PCN exhibits a breakthrough photocatalytic H_2O_2 generation performance with the H_2O_2 production rate of $16.01 \text{ mmol} \cdot \text{L}^{-1} \cdot \text{h}^{-1} \cdot \text{g}^{-1}$ under visible light ($\lambda > 400 \text{ nm}$) (Fig. 3a).

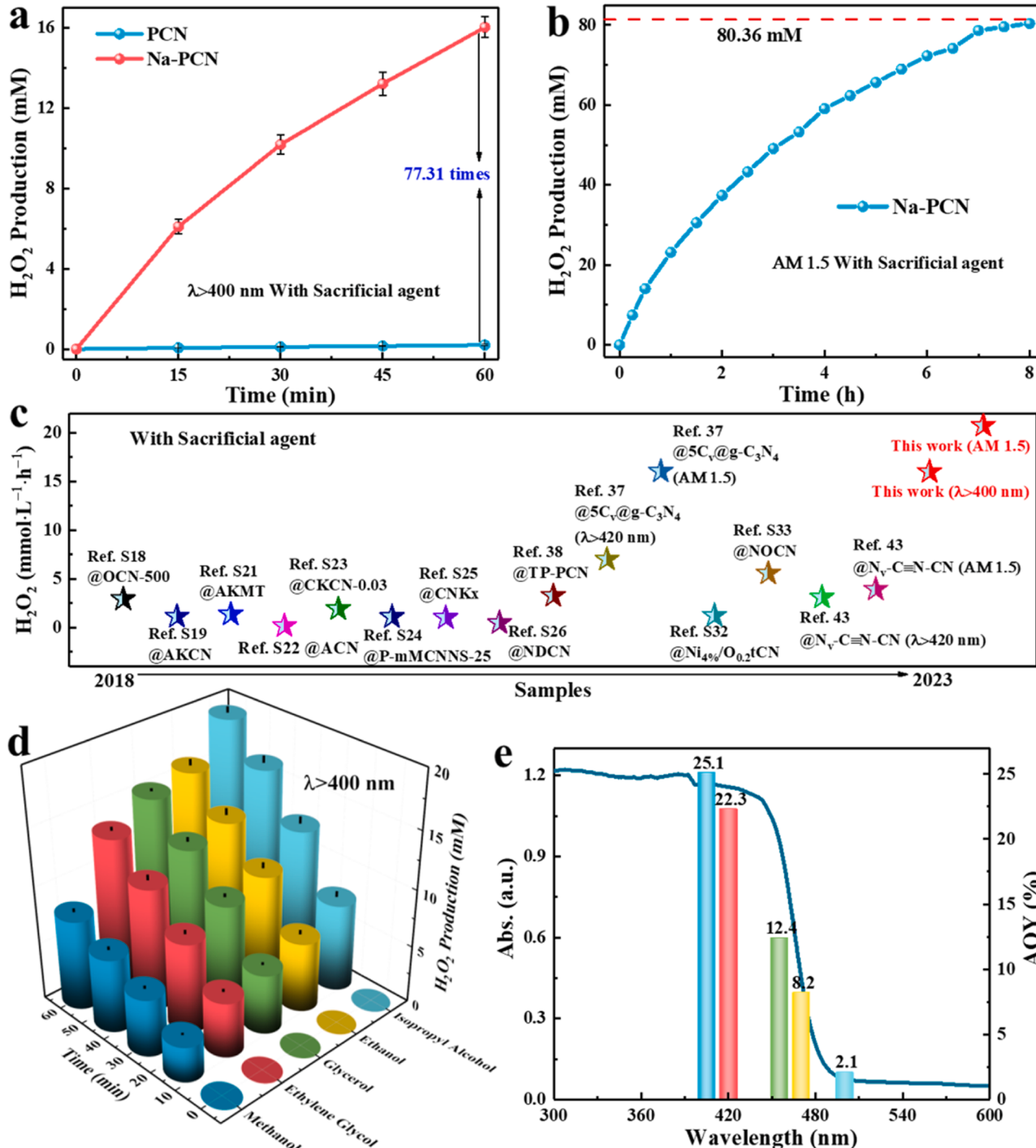


Fig. 3. (a) Photocatalytic H_2O_2 generation efficiency of PCN and Na-PCN; (b) H_2O_2 concentration after reaction 8 h under simulated sunlight (AM1.5); (c) Comparison of photocatalytic H_2O_2 production performance with state-of-the-art photocatalysts from recent work, more details of which can be found in Table S4 in the Supporting Information; (d) Photocatalytic H_2O_2 production performance of Na-PCN under different sacrificial agents; (e) The apparent quantum efficiency (AQY) of Na-PCN at different wavelengths (isopropanol as sacrificial agent).

Here, iodometry was used to determine the H_2O_2 production rate (Fig. S12). Significantly, comparing the performance with the most advanced photocatalysts reported in recent literature work, it was found that the Na-PCN photocatalyst exhibited the optimal photocatalytic H_2O_2 production performance (Fig. 3c), and more details are shown in Table S4. Further, compared with the PCN, the Na-PCN obtained by calcination at different temperatures all exhibited excellent photocatalytic H_2O_2 production performance (Fig. S13). Meanwhile, the H_2O_2 concentration reached 68.27 mM after reaction 6 h (S14a). In addition, the optimized Na-PCN further exhibited an H_2O_2 generation rate of $20.76 \text{ mmol}\cdot\text{L}^{-1}\cdot\text{h}^{-1}\cdot\text{g}^{-1}$ under simulated sunlight (AM 1.5) (Fig. S14c). Meanwhile, the H_2O_2 concentration reached 80.36 mM after reaction 8 h (Fig. 3b), which was closely related to the high conversion efficiency of O_2 to H_2O_2 .

The decomposition experiments of H_2O_2 on the catalyst surface showed (Fig. S14d) that the continuous accumulation of H_2O_2 resulted

from the low decomposition rate of H_2O_2 , indicating that the high crystalline Na-PCN promoted the production and inhibited the decomposition of H_2O_2 . The effects of NaCl templating agent dosage and solution pH (Fig. S15–16) on the photocatalytic H_2O_2 generation efficiency were also investigated, and the results showed that Na-PCN exhibited millimolar generation rates of H_2O_2 . With different sacrificial agents, the rate of H_2O_2 generation reached $19.21 \text{ mmol}\cdot\text{L}^{-1}\cdot\text{h}^{-1}\cdot\text{g}^{-1}$ when isopropanol was used as sacrificial agent (Fig. 3d). The photocatalytic H_2O_2 yield in the absence of sacrificial agents ($133.48 \text{ mmol}\cdot\text{L}^{-1}\cdot\text{h}^{-1}\cdot\text{g}^{-1}$) was 4.0 times higher than that of PCN (Fig. S17a and Table S2), as well as the H_2O_2 generation rate reached $155.37 \text{ mmol}\cdot\text{L}^{-1}\cdot\text{h}^{-1}\cdot\text{g}^{-1}$ under simulated sunlight. To evaluate the light utilization efficiency of Na-PCN, the apparent quantum efficiency (AQY) under different monochromatic light irradiation was tested (Fig. 3e and S17b). The AQY of Na-PCN at 405 nm and 420 nm under isopropyl alcohol as a sacrificial agent reached 25.1% and 22.3%,

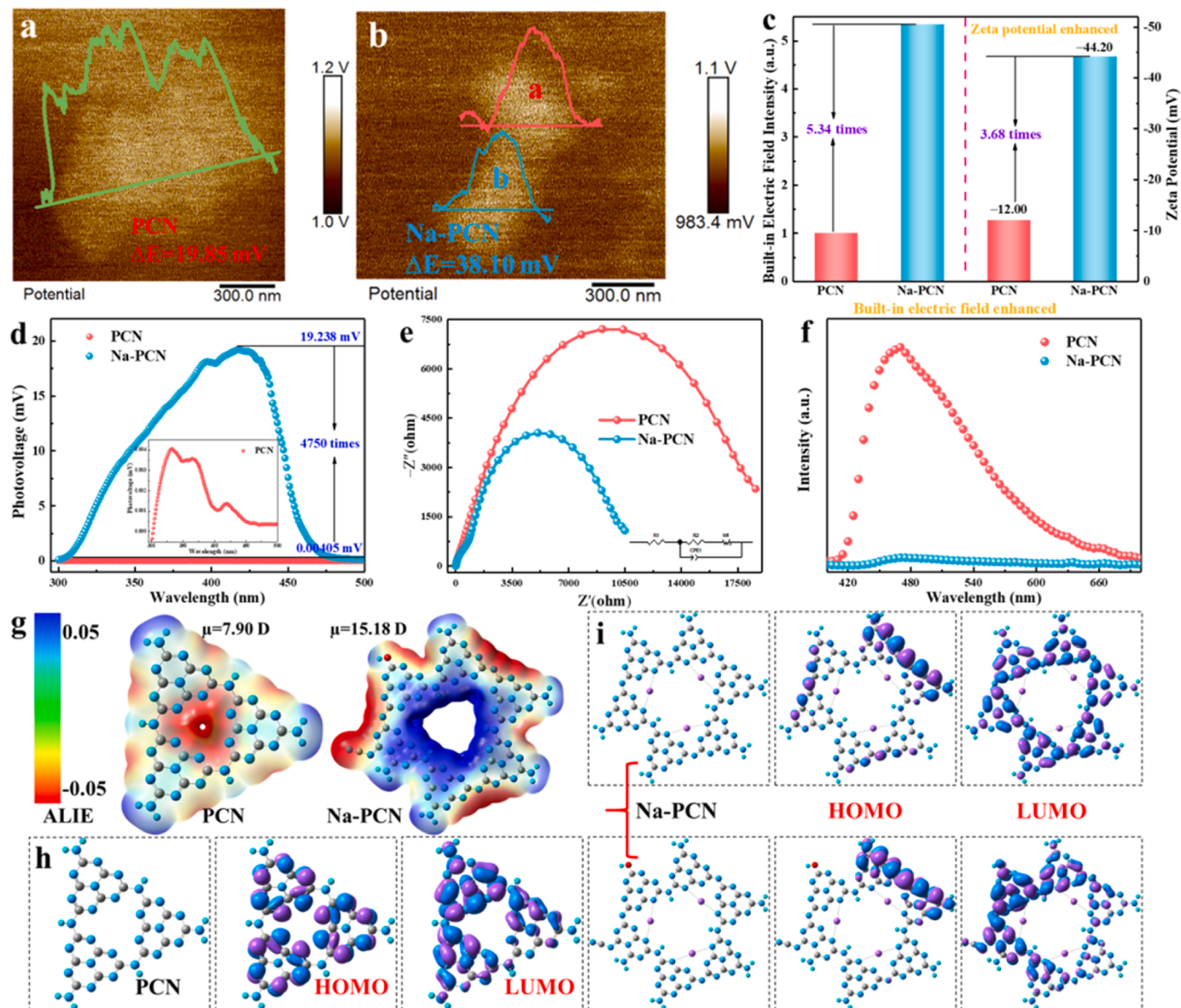


Fig. 4. (a) and (b) Surface potentials of PCN and Na-PCN with the Kelvin probe force microscopy (KPFM), respectively; (c) The built-in electric field intensity and zeta potential of PCN and Na-PCN; (d), (e) and (f) Surface photovoltage (SPV), electrochemical impedance spectra (EIS) and photoluminescence (PL) spectra of PCN and Na-PCN, respectively; (g) Electrostatic potential (ESP) charge density distributions of optimized PCN and Na-PCN; (h) and (i) Electronic structures of LUMO and HOMO of the optimized PCN and Na-PCN. The cyan and purple denominations represent electron and hole distribution, respectively. The equivalent face value is $0.015 \text{ e}/\text{\AA}^3$. Blue, gray, cyan and purple represent the N, C, H and Na elements, respectively.

respectively (Fig. 3e and Table S2). In addition, Na-PCN exhibited good cyclability (Fig. S18) and stability (Fig. S19–20) for photocatalytic generation of H₂O₂. The high photocatalytic performance of highly crystalline Na-PCN can be demonstrated not only in efficient H₂O₂ production, but also in efficient biomass conversion and pollutant degradation (Figs. S21–S22). The results indicate that Na-PCN is a highly active photocatalyst for photocatalytic environmental remediation and energy conversion.

3.3. Strong built-in electric field and high charge separation efficiency

The kinetic factors for the enhanced performance of Na-PCN were revealed by the charge separation efficiency. The efficient charge separation and migration is beneficial to generate high surface charge density, which promotes the catalyst surface redox reactions on the catalyst surface. The strong built-in electric field induced by its high crystallinity helps to induce exciton dissociation and promotes the effective separation of photogenerated charges. Meanwhile, the formed nanocrystals shorten the charge migration distance to facilitate the rapid migration of photogenerated charges. The built-in electric field intensity is proportional to the square root of the product of the surface charge density and the surface potential [44–46]. The surface potential was measured by Kelvin probe force microscopy (KPFM), and the surface charge density is proportional to the zeta potential [47–49]. The surface potential (ΔE) (Fig. 4a-b and S23) of Na-PCN ($\Delta E = 38.10$ mV) is much higher than that of PCN ($\Delta E = 19.85$ mV) and high surface charge density distribution (Fig. S24). In addition, the zeta potential of Na-PCN (-44.20 mV) was measured to be 3.68 times larger than that of PCN (-12.00 mV) (Fig. 4c). In addition, the built-in electric field intensity of Na-PCN was quantified by the photogenerated charge density and open-circuit potential (OCPT) (Fig. S25) to be 5.34 times higher than that of PCN (Fig. 4c). As a result, Na-PCN exhibits stronger photocurrent (Fig. S25b) and surface photovoltage (SPV) (Fig. 4d), where the resulting photovoltage is 4750 times higher than that of PCN, demonstrating that Na-PCN generates high surface charge density. Besides, Na-PCN exhibited a smaller EIS arc radius (Fig. 4e), lower photoluminescence (PL) intensity (Fig. 4f) and shorter fluorescence lifetime (Fig. S26 and Table S3), further confirming that Na-PCN has a faster photogenerated carrier migration rate. The results show that the strong built-in electric field greatly promotes the separation and migration of photogenerated charges. Meanwhile, the photogenerated electrons rapidly migrate to the catalyst surface to participate in the 2e[−] O₂ reduction reaction.

To reveal the key role of surface –OH/–C≡N groups in surface reactions, we investigate the charge density distribution of different structures by density functional theory (DFT). The introduction of –OH/–C≡N groups with the electronegativity difference has a significant effect on the electron distribution and dipole of the catalyst. According to the ESP distribution (Fig. 4g), the introduction of –OH/–C≡N groups into Na-PCN produces a larger dipole moment and a significant potential difference, which facilitates the provision of more reactive sites and generates a high surface charge density [50,51]. We also calculated the charge density distributions of the highest occupied molecular orbital (HOMO) and the lowest unoccupied molecular orbital (LUMO) of the catalyst structure by DFT. The charge densities of HOMO and LOMO are more uniformly distributed for PCN (Fig. 4h). However, the introduction of –OH/–C≡N groups into Na-PCN leads to a more localized spatial distribution of charge density, which may be an important reason for the generation of high charge separation efficiency (Fig. 4i) [52,53]. The electronic configuration of the LUMO can almost represent the photogenerated electronic configuration [54]. Interestingly, the charge of LUMO is more concentrated on the –OH/–C≡N site, suggesting that the –OH/–C≡N site acts as a reduction site for O₂. It should be noted that the local distribution of charge density facilitates the separation of reduction and oxidation sites and effectively drives the effective surface reaction of electrons and holes [52]. The high charge separation efficiency and surface charge density are intrinsic to the efficient

photocatalytic H₂O₂ production under visible light. On the contrary, the ability to capture visible light and the energy band structure were not the main reasons affecting the efficient photocatalytic H₂O₂ production (Figs. S27–S29).

3.4. Mechanism of efficient photocatalytic H₂O₂ generation

To investigate the mechanism of H₂O₂ production by the 2e[−] ORR reaction, the number of electrons transferred (n) and the selectivity of H₂O₂ production were investigated using rotating disk electrodes (RRDE) (Fig. S30). Compared to PCN, Na-PCN exhibited closer two-electron reduction reaction and higher selectivity for H₂O₂ production. To illustrate the surface –C≡N/–OH groups as an adsorption site for O₂, the possible adsorption active sites and the adsorption free energy of O₂ in both models were calculated by DFT (Figs. S31 and 5a-b), which confirmed that the adsorption of O₂ at the –OH/–C≡N sites was more favorable than other positions. The strong adsorption capacity of Na-PCN for O₂ was further confirmed by TPD-O₂ (Fig. 5c). In addition, the high dispersibility and hydrophilicity of Na-PCN facilitate the adsorption of O₂ and H⁺ in the aqueous phase. The zeta potential test (Fig. 5d) showed that Na-PCN exhibited a more negative zeta potential compared to PCN, which was favorable for the adsorption of H⁺ in solution and accelerated the combination with reactive oxygen species to form H₂O₂. To verify the mechanism of H₂O₂ formation, activity experiments under different atmospheres and active species trapping experiments were performed. The experiments under different atmospheres proved that O₂ is a necessary reactant (Fig. 4e and S32a-b). Meanwhile, it was also confirmed that the photo-reduced Na-PCN could store the trapped electrons and achieve O₂ reduction to H₂O₂ during the dark reaction (Fig. S33). Furthermore, when AgNO₃ was added to the reaction system (Fig. 5e), the yield of H₂O₂ decreased sharply, indicating that the formation of H₂O₂ originated from the photogenerated electron reduction of O₂ (Fig. S32c). Significantly, the superoxide radical (•O₂[−]) trapping experiments confirmed that the •O₂[−] is a necessary intermediate for H₂O₂ production (Fig. S32c-d). The presence of the •O₂[−] was further confirmed by EPR trapping experiments of 5,5-dimethyl-1-pyrrolidine N-oxide (DMPO) (Fig. 5f). Meanwhile, Na-PCN exhibited 72.7 times the •O₂[−] EPR signal intensity relative to PCN, indicating that Na-PCN is more favorable for rapid H₂O₂ production. The above results confirm the formation of the •O₂[−] intermediate species and the 2e[−] synthesis pathway.

In-situ Fourier transform infrared (in-situ FT-IR) spectroscopy is an effective method to study the exact mechanism of photocatalysis. The FT-IR spectra of photocatalytic H₂O₂ production by the Na-PCN photocatalytic system were studied in aqueous solution and continuous O₂ flow (Fig. 5g-h and S34). The bands located at 1278, 1362 and 840 cm^{−1} intensities at the prolonged irradiation time intervals, which can be respectively attributed to the O–O stretching mode of surface-adsorbed superoxide *OOH, the OOH bending mode of surface-adsorbed hydroperoxide *HOOH and the O–O stretch of hydroperoxide (HO–OH), respectively, indicating the formation of H₂O₂ on the surface of Na-PCN via a superoxide intermediate pathway [55,56]. Meanwhile, the characteristic peaks at 946 and 1156 cm^{−1} ascribed to O–O bonding and •O₂[−] in this spectrum also gradually increased [57–59]. In addition, the band at 1103 and 1434 cm^{−1} in FT-IR spectra can be attributed to C–OH and C–O, indicating that the OH* is an important intermediate species in the formation process of H₂O₂ [62]. All of the above findings confirm the formation of •O₂[−] and *OOH intermediate species and the 2e[−] two-step synthesis route. At the same time, the peak at 3260 cm^{−1} assigned to the N–H stretching vibration and the intensity gradually decreased with the longer irradiation time intervals, which can be attributed to the consumption of hydrogen protons adsorbed on the catalyst surface [60]. Interestingly, the characteristic peak at about 802 cm^{−1} is attributed to the respiration pattern of the triazine structure in the heptazine fraction, confirming the redox reaction process on heptazine [61]. Furthermore, the detection of a weaker FT-IR signal

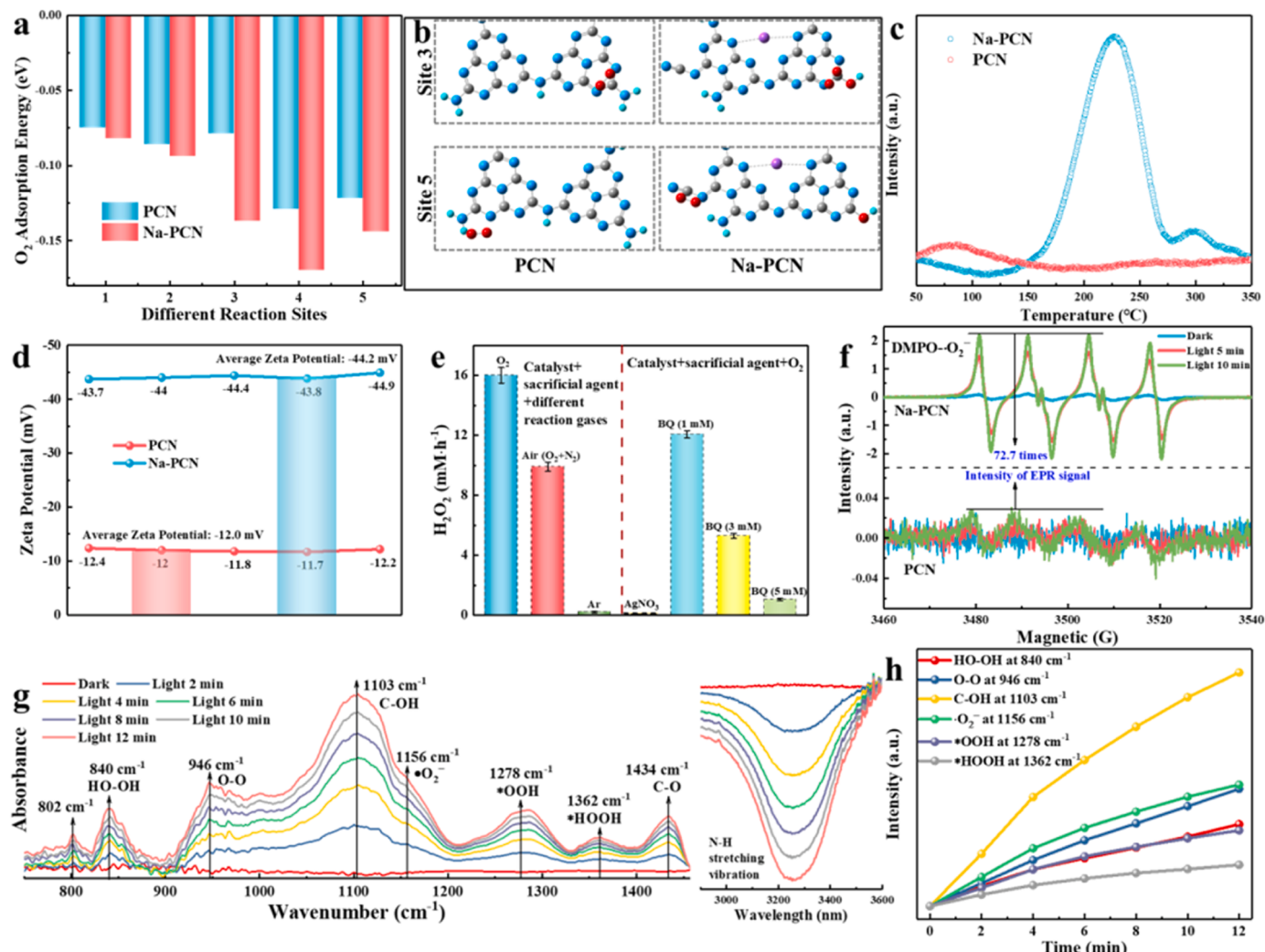


Fig. 5. (a) and (b) Free energy of oxygen adsorption (E_{ads}) at different adsorption sites and adsorption sites for PCN and Na-PCN by DFT; (c) Temperature programmed O_2 desorption (TPD- O_2) profiles of PCN and Na-PCN; (d) The Zeta potentials of PCN and Na-PCN; (e) Photocatalytic H_2O_2 production performance of Na-PCN under different reaction gases, electron trapping agent ($AgNO_3$) and superoxide radical trapping agent (p-benzoquinone); (f) Superoxide radical electron paramagnetic resonance (EPR) signals of PCN and Na-PCN; (g) In-situ FT-IR spectra of Na-PCN at 750–1450 cm⁻¹ and 2900–3600 cm⁻¹ during the photocatalytic H_2O_2 generation in pure water; (h) The intensity of the peaks at 840, 946, 1103, 1156, 1278 and 1362 cm⁻¹ vs illumination time.

peak in the aqueous ethanol solution (Fig. S35) suggests that ethanol acts as a sacrificial agent to accelerate the conversion O_2 to H_2O_2 , and also confirms that the aqueous oxidation process is the crucial step for photocatalytic H_2O_2 production in pure water.

Based on the above results, it is evident that the high charge separation efficiency and the abundant surface-active sites are intrinsic to the efficient photocatalytic H_2O_2 production under visible light. Under visible light irradiation, photons excite Na-PCN to generate electron-hole pairs, and the strong built-in electric field accelerates the directional transfer of photogenerated electrons to the surface-active sites. The surface $-OH/-C\equiv N$ sites effectively adsorb O_2 , while promoting the adsorption of H^+ on the catalyst surface and coupling with oxygen-active species to form H_2O_2 . The strong built-in electric field provided excellent two-electron O_2 reduction selectivity and catalytic activity, which significantly promoted the efficiency of H_2O_2 generation.

4. Conclusion

A highly crystalline Na-PCN with the strong built-in electric field and the abundant surface $-C\equiv N/-OH$ groups was prepared. Meanwhile, the π -conjugated structure and high crystallinity of Na-PCN contribute

to the enhancement of the built-in electric field for accelerating exciton dissociation and photogenerated carrier separation and rapid migration, resulting in a high surface charge density. Meanwhile, the formed nanocrystals shorten the charge migration distance to facilitate photogenerated charge rapid migration. The abundant surface $-C\equiv N/-OH$ groups provide more surface-active sites for the adsorption reduction of O_2 . Therefore, the photocatalytic H_2O_2 production rate reached $16.01 \text{ mmol} \cdot \text{L}^{-1} \cdot \text{h}^{-1} \cdot \text{g}^{-1}$ under visible light, with a quantum efficiency of 25.1% at 405 nm. The H_2O_2 concentration reached 80.36 mM after 8 h reaction under simulated sunlight. This study provides a new insight into the design of photocatalytic systems with high crystallinity and the strong built-in electric field and insight into the mechanism of photocatalytic $2e^-$ ORR reaction for H_2O_2 production.

CRediT authorship contribution statement

L. Jian, Y.M. Dong, H. Zhao, C.S. Pan and Y.F. Zhu for Data curation, Formal analysis and draft writing of materials and photocatalytic performance. L. Jian, Y.M. Dong, G.L. Wang and Y.F. Zhu for Data curation and Formal analysis and draft writing of charge separation/transfer kinetics. L. Jian, Y.M. Dong, and H. Zhao for Data

curation and Formal analysis and draft writing of the first-principle calculation based on the Density Functional Theory.

Declaration of Competing Interest

The authors declare that they have no known competing financial interests or personal relationships that could have appeared to influence the work reported in this paper.

Data Availability

Data will be made available on request.

Acknowledgements

The work is supported by the National Natural Science Foundation of China (22136002, 22172064, 22376083), Special Fund Project of Jiangsu Province for Scientific and Technological Innovation in Carbon Peaking and Carbon Neutrality (BK20220023) and Fundamental Research Funds for the Central Universities (JUSPR122020).

Appendix A. Supporting information

Supplementary data associated with this article can be found in the online version at [doi:10.1016/j.apcatb.2023.123340](https://doi.org/10.1016/j.apcatb.2023.123340).

References

- [1] G. h Moon, M. Fujitsuka, S. Kim, T. Majima, X. Wang, W. Choi, *ACS Catal.* 7 (2017) 2886.
- [2] Y. Sun, L. Han, P. Strasser, *Chem. Soc. Rev.* 49 (2020) 6605.
- [3] H. Hou, X. Zeng, X. Zhang, *Angew. Chem. Int. Ed. Engl.* 59 (2020) 17356.
- [4] Z. Teng, Q. Zhang, H. Yang, K. Kato, W. Yang, Y.R. Lu, S. Liu, C. Wang, A. Yamakata, C. Su, B. Liu, T. Ohno, *Nat. Catal.* 4 (2021) 374.
- [5] Y. Zhang, C. Pan, G. Bian, J. Xu, Y. Dong, Y. Zhang, Y. Lou, W. Liu, Y. Zhu, *Nat. Energy* 8 (2023) 361.
- [6] T. Liu, Z. Pan, J.J.M. Vequizo, K. Kato, B. Wu, A. Yamakata, K. Katayama, B. Chen, C. Chu, K. Domen, *Nat. Commun.* 13 (2022) 1034.
- [7] J. Ma, X. Peng, Z. Zhou, H. Yang, K. Wu, Z. Fang, D. Han, Y. Fang, S. Liu, Y. Shen, Y. Zhang, *Angew. Chem. Int. Ed. Engl.* 61 (2022), 202210856.
- [8] C. Pan, G. Bian, Y. Zhang, Y. Lou, Y. Zhang, Y. Dong, J. Xu, Y. Zhu, *Appl. Catal. B: Environ.* 316 (2022), 121675.
- [9] W. Zhao, P. Yan, B. Li, M. Bahri, L. Liu, X. Zhou, R. Clowes, N.D. Browning, Y. Wu, J.W. Ward, A.I. Cooper, *J. Am. Chem. Soc.* 144 (2022) 9902.
- [10] C. Wu, Z. Teng, C. Yang, F. Chen, H.B. Yang, L. Wang, H. Xu, B. Liu, G. Zheng, Q. Han, *Adv. Mater.* 34 (2022), 2110266.
- [11] S. Wu, X. Quan, *ACS EST Eng.* 2 (2022) 1068.
- [12] Y. Ding, S. Maitra, S. Halder, C. Wang, R. Zheng, T. Barakat, S. Roy, L.H. Chen, B. L. Su, *Matter* 5 (2022) 2119.
- [13] H. Cheng, J. Cheng, L. Wang, H. Xu, *Chem. Mater.* 34 (2022) 4259.
- [14] H. Wang, S. Jiang, S. Chen, X. Zhang, W. Shao, X. Sun, Z. Zhao, Q. Zhang, Y. Luo, Y. Xie, *Chem. Sci.* 8 (2017) 4087.
- [15] J. Zhang, J. Sun, K. Maeda, K. Domen, P. Liu, M. Antonietti, X. Fu, X. Wang, *Energy Environ. Sci.* 4 (2011) 675.
- [16] S. Brazovskii, N. Kirova, *Chem. Soc. Rev.* 39 (2010) 2453.
- [17] A.J. Heeger, *Chem. Soc. Rev.* 39 (2010) 2354.
- [18] S. Melissen, T. Le Bahers, S.N. Steinmann, P. Sautet, *J. Phys. Chem. C.* 119 (2015) 25188.
- [19] F. Guo, B. Hu, C. Yang, J. Zhang, Y. Hou, X. Wang, *Adv. Mater.* 33 (2021), 2101466.
- [20] G. Zhang, J. Zhu, Y. Xu, C. Yang, C. He, P. Zhang, Y. Li, X. Ren, H. Mi, *ACS Catal.* 12 (2022) 4648.
- [21] Y. Kang, Y. Yang, L.C. Yin, X. Kang, L. Wang, G. Liu, H.M. Cheng, *Adv. Mater.* 28 (2016) 6471.
- [22] B. Yan, C. Du, G. Yang, *Small* 16 (2020), 1905700.
- [23] G. Zhang, Y. Xu, D. Yan, C. He, Y. Li, X. Ren, P. Zhang, H. Mi, *ACS Catal.* 11 (2021) 6995.
- [24] J. Zhang, X. Liang, C. Zhang, L. Lin, W. Xing, Z. Yu, G. Zhang, X. Wang, *Angew. Chem. Int. Ed. Engl.* 61 (2022), 202210849.
- [25] X. Ruan, C. Huang, H. Cheng, Z. Zhang, Y. Cui, Z. Li, T. Xie, K. Ba, H. Zhang, L. Zhang, X. Zhao, J. Leng, S. Jin, W. Zhang, W. Zheng, S.K. Ravi, Z. Jiang, X. Cui, J. Yu, *Adv. Mater.* 35 (2023), 2209141.
- [26] J. Xu, Q. Gao, Z. Wang, Y. Zhu, *Appl. Catal. B: Environ.* 291 (2021), 120059.
- [27] Z. Zhu, Q. Lv, Y. Ni, S. Gao, J. Geng, J. Liang, F. Li, *Angew. Chem. Int. Ed. Engl.* 61 (2022), 202116699.
- [28] Q. Zhou, Y. Guo, Z. Ye, Y. Fu, Y. Guo, Y. Zhu, *Mater. Today* 58 (2022) 100.
- [29] L. Jian, H. Zhao, Y. Dong, J. Xu, Q. Mao, R. Ji, Z. Yan, C. Pan, G. Wang, Y. Zhu, *Catal. Sci. Technol.* 12 (2022) 7379.
- [30] S. Song, C. Lu, X. Wu, S. Jiang, C. Sun, Z. Le, *Appl. Catal. B: Environ.* 227 (2018) 145.
- [31] F. Guo, S. Li, Y. Hou, J. Xu, S. Lin, X. Wang, *Chem. Commun. (Camb.)* 55 (2019) 11259.
- [32] M.A.R. da Silva, I.F. Silva, Q. Xue, B.T.W. Lo, N.V. Tarakina, B.N. Nunes, P. Adler, S.K. Sahoo, D.W. Bahnemann, N. López-Salas, A. Savateev, C. Ribeiro, T.D. Kühne, M. Antonietti, I.F. Teixeira, *Appl. Catal. B: Environ.* 304 (2022), 120965.
- [33] A. Savateev, N.V. Tarakina, V. Strauss, T. Hussain, K. Ten Brummelhuis, J. M. Sanchez Vadillo, Y. Markushyna, S. Mazzanti, A.P. Tyutyunnik, R. Walczak, M. Oschatz, D.M. Guldin, A. Karton, M. Antonietti, *Angew. Chem. Int. Ed. Engl.* 59 (2020) 15061.
- [34] I.F. Teixeira, N.V. Tarakina, I.F. Silva, N. López-Salas, A. Savateev, M. Antonietti, *Adv. Sustain. Syst.* 6 (2022), 2100429.
- [35] Z. Chen, A. Savateev, S. Pronkin, V. Papaefthimiou, C. Wolff, M.G. Willinger, E. Willinger, D. Neher, M. Antonietti, D. Dontsova, *Adv. Mater.* 29 (2017), 1700555.
- [36] H. Schlomberg, J. Kroger, G. Savasci, M.W. Terban, S. Bette, I. Moudrakovski, V. Duppel, F. Podjaski, R. Siegel, J. Senker, R.E. Dinnebier, C. Ochsenfeld, B. V. Lotsch, *Chem. Mater.* 31 (2019) 7478.
- [37] L. Chen, C. Chen, Z. Yang, S. Li, C. Chu, B. Chen, *Adv. Funct. Mater.* 31 (2021), 2105731.
- [38] H. Che, X. Gao, J. Chen, J. Hou, Y. Ao, P. Wang, *Angew. Chem. Int. Ed. Engl.* 60 (2021) 25546.
- [39] J. Jiang, L. Ou-yang, L. Zhu, A. Zheng, J. Zou, X. Yi, H. Tang, *Carbon* 80 (2014) 213.
- [40] J. Li, B. Shen, Z. Hong, B. Lin, B. Gao, Y. Chen, *Chem. Commun. (Camb.)* 48 (2012) 12017.
- [41] P. Sharma, T.J.A. Slater, M. Sharma, M. Bowker, C.R.A. Catlow, *Chem. Mater.* 34 (2022) 5511.
- [42] P.V. Zinin, L.-C. Ming, S.K. Sharma, V.N. Khabashesku, X. Liu, S. Hong, S. Endo, T. Acosta, *Chem. Phys. Lett.* 472 (2009) 69.
- [43] X. Zhang, P. Ma, C. Wang, L. Gan, X. Chen, P. Zhang, Y. Wang, H. Li, L. Wang, X. Zhou, K. Zheng, *Energy Environ. Sci.* 15 (2022) 830.
- [44] X. Chen, J. Wang, Y. Chai, Z. Zhang, Y. Zhu, *Adv. Mater.* 33 (2021), 2007479.
- [45] Y. Sheng, W. Li, L. Xu, Y. Zhu, *Adv. Mater.* 34 (2022), 2102354.
- [46] Z. Zhang, X. Chen, H. Zhang, W. Liu, W. Zhu, Y. Zhu, *Adv. Mater.* 32 (2020), 1907746.
- [47] Y. Guo, Q. Zhou, J. Nan, W. Shi, F. Cui, Y. Zhu, *Nat. Commun.* 13 (2022) 2067.
- [48] J. Xu, W. Li, W. Liu, J. Jing, K. Zhang, L. Liu, J. Yang, E. Zhu, J. Li, Y. Zhu, *Angew. Chem. Int. Ed. Engl.* 61 (2022), 202212243.
- [49] J. Jing, J. Yang, W. Li, Z. Wu, Y. Zhu, *Adv. Mater.* 34 (2022), 2106807.
- [50] J. Yang, J. Jing, W. Li, Y. Zhu, *Adv. Sci. (Weinh.)* 9 (2022), 2201134.
- [51] Z. Zhang, Y. Zhu, X. Chen, H. Zhang, J. Wang, *Adv. Mater.* 31 (2019), 1806626.
- [52] D. Zhao, C.L. Dong, B. Wang, C. Chen, Y.C. Huang, Z. Diao, S. Li, L. Guo, S. Shen, *Adv. Mater.* 31 (2019), 1903545.
- [53] Y. Wang, P. Du, H. Pan, L. Fu, Y. Zhang, J. Chen, Y. Du, N. Tang, G. Liu, *Adv. Mater.* 31 (2019), 1807540.
- [54] L. Su, P. Wang, X. Ma, J. Wang, S. Zhan, *Angew. Chem. Int. Ed. Engl.* 133 (2021) 21431.
- [55] S. Nayak, I.J. McPherson, K.A. Vincent, *Angew. Chem. Int. Ed. Engl.* 57 (2018) 12855.
- [56] J. Luo, X. Wei, Y. Qiao, C. Wu, L. Li, L. Chen, J. Shi, *Adv. Mater.* 35 (2023), 2210110.
- [57] H. Liu, Z. Zhang, J. Fang, M. Li, M.G. Sendeku, X. Wang, H. Wu, Y. Li, J. Ge, Z. Zhuang, D. Zhou, Y. Kuang, X. Sun, *Joule* 7 (2023) 558.
- [58] X. Wang, X. Yang, C. Zhao, Y. Pi, X. Li, Z. Jia, S. Zhou, J. Zhao, L. Wu, J. Liu, *Angew. Chem. Int. Ed. Engl.* (2023), 202302829.
- [59] Q. Zhi, W. Liu, R. Jiang, X. Zhan, Y. Jin, X. Chen, X. Yang, K. Wang, W. Cao, D. Qi, J. Jiang, *J. Am. Chem. Soc.* 144 (2022) 21328.
- [60] M. Kou, Y. Wang, Y. Xu, L. Ye, Y. Huang, B. Jia, H. Li, J. Ren, Y. Deng, J. Chen, Y. Zhou, K. Lei, L. Wang, W. Liu, H. Huang, T. Ma, *Angew. Chem. Int. Ed. Engl.* 61 (2022), 202200413.
- [61] H. Cheng, H. Lv, J. Cheng, L. Wang, X. Wu, H. Xu, *Adv. Mater.* 34 (2022), 2107480.
- [62] C. Zhao, X.Y. Wang, Y.F. Yin, W.M. Tian, G. Zeng, H.T. Li, S. Ye, L.M. Wu, J. Liu, *Angew. Chem. Int. Ed. Engl.* 62 (2023), 202218318.